Editors' Suggestion

Stratified shear instability in the cabbeling regime

Taylor Hanson, Marek Stastna, and Aaron Coutino
Department of Applied Mathematics, University of Waterloo, Waterloo, Ontario, Canada

(Received 20 August 2020; accepted 1 July 2021; published 5 August 2021)

The shear instability of stratified fluids is a well-studied problem in transition to turbulence. In temperate lakes, early springs typically lead to a weak thermal stratification involving water both above and below the temperature at which the density maximum occurs. This implies that mixing of two parcels with the same density, but different temperature, can lead to the creation of denser fluid, a phenomenon known as cabbeling. We report on simulations of shear instability in the cabbeling regime. We find that the initial stages of instability are dominated by shear instability, yielding billows. However, these billows are systematically located below the centerline of the shear layer. Three-dimensionalization occurs through Rayleigh-Taylor-like instabilities, and cabbeling efficiency is greatly increased in the fully three-dimensionalized state. By contrasting with initial states that have the same density profile, but a temperature well outside of the cabbeling regime, we demonstrate that the fully three-dimensional state of the density field is fundamentally different in the cabbeling regime.

DOI: 10.1103/PhysRevFluids.6.084802

I. INTRODUCTION

Stratified shear instability has provided fertile ground for a variety of fluid mechanics subdisciplines. In [1] Hazel provides an early example of a successful application of numerical methods to hydrodynamic stability, while the transition to turbulence in stratified shear flows via secondary instabilities has led to an active literature spanning several decades [2–6]. In the past few years, a considerable focus has been on the distinction between Kelvin-Helmholtz-type instability and Holmboe-type instability [7,8], with the latter allowing for long-term maintenance of a stratified layer that is disturbed by "tearing" events. Both types of instability have been observed in the natural world [9,10] and continue to drive fundamental progress in theoretical nonlinear physics [8,11].

It is well known that the equation of state for temperature stratified water is nonmonotonic in the cold water regime, as shown in Fig. 1. The temperature of maximum density, typically 4 °C, is denoted by T^* with a corresponding density $\rho_{\max} = \rho(T^*) = 1000$ kg m^{-3}. The $\rho(T)$ curve near T^* is essentially quadratic. This implies that it is possible to mix fluids of two identical densities (but different temperatures) to produce denser fluid, a phenomenon known as cabbeling. Cabbeling can also occur in the context of seawater; see [12] for a recent reference. The typical density differences (or their dimensionless counterpart, the Atwood number, $\mathrm{At} = (\rho_{\max} - \rho_{\min})/2\rho_0$) in the cold water regime are small. The low Atwood regime of stratified instabilities has received attention in the past [13]; however, the typical Atwood numbers in the cold water regime are in fact even lower ($\approx 5 \times 10^{-5}$). While phenomena occurring at warmer temperatures typically involve higher values of the Atwood number, a phenomenon with a range of temperatures, $0 < T < T^*$, can be realized with the same strength of buoyancy for warmer water, near T^{high}. However, the range of temperature values would have to be much smaller [i.e., the slope of the $\rho(T)$ curve is much larger, and negative, for warm water as seen in Fig. 1].

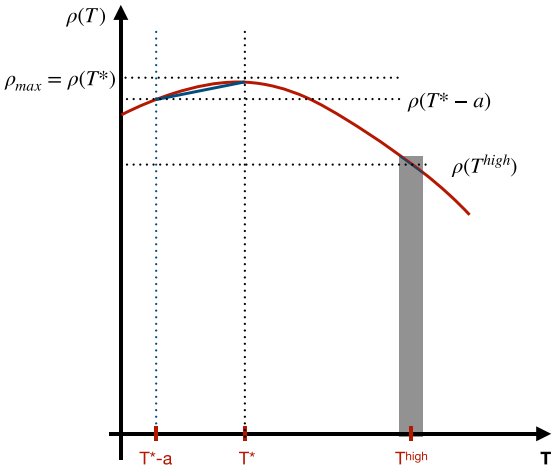

FIG. 1. The density of pure water as a function of temperature. The temperature of highest density is labeled T^*. A typical density difference for cold water is labeled in blue. The gray rectangle indicates a range of temperatures outside the cabbeling regime with the same density difference as $\rho(T^* - a) - \rho(T^*)$.

The cabbeling regime for water is not just of theoretical interest. Each winter, in temperate and cold climate lakes, the water cools to reach a stable, inverse (temperature increasing with depth) stratification. At this point the entire water column is below T^*, save for possibly a small region near the lake bed (see Kirillin *et al.* [14] their Fig. 9(b)). As the solar insolation strengthens after the winter solstice, and especially early in the springtime when lakes are still covered by ice, the water heats up, yielding overturning before a stably stratified regime is reached. As an example, recent measurements in Lake Simcoe, Canada [15] provide an example of under ice convection in late winter and early spring, as well as implications for the spatial distribution of dissolved oxygen. While our focus will be on smaller scales than the sampling work of Yang *et al.* [15], it is worth noting that simulations in this regime have a long history. Cooper [16], Vasseur and Robillard [17], and Lin and Nansteel [18], all looked at the onset of natural convection of sub-4 °C water in an enclosure. These papers presented the overarching convection mechanisms but considered only very small grids by modern computational standards. Recent two-dimensional (2D) simulations by Ulloa *et al.* [19] have revisited this problem on the scale of a small lake. While these authors' model is complex, involving an embedded boundary and hence a form of downslope flow, the primary message of their study is in setting the velocity scale [see their inset of Fig. 1(c) [19]] as roughly 1 cm s^{-1} with length scales of variability on the order of 10 cm. It is thus important to revisit cabbeling phenomena at a modest Reynolds number in a well-resolved direct numerical simulation (henceforth DNS), especially since it has been shown that irreversible mixing during shear instability is fundamentally different in three dimensions [20]. As an aside, the well-known adiabatic sorting algorithm used to define the background and available potential energy in [20] (and similar papers) does not have a clear counterpart in the presence of cabbeling (where mixing of two fluid parcels with identical density can yield higher densities). Thus, when we discuss "mixing" we do so in terms of changes in the gradients of the temperature field (which in turn sets the density through the nonmonotonic equation of state).

In this paper, we address freshwater cabbeling specifically, although it is worth mentioning that seawater cabbeling is a more general phenomenon. In the context of seawater, cabbeling is often discussed on much larger scales of motion and involves the complex manner in which density depends on both salinity and temperature [i.e., $\rho(T, s)$]. The previously mentioned paper [12] discusses water mass transformation on global scales. Cabbeling is thus an invoked mechanism, with the underlying data being based on climatology. The distribution of cabbeling in the global

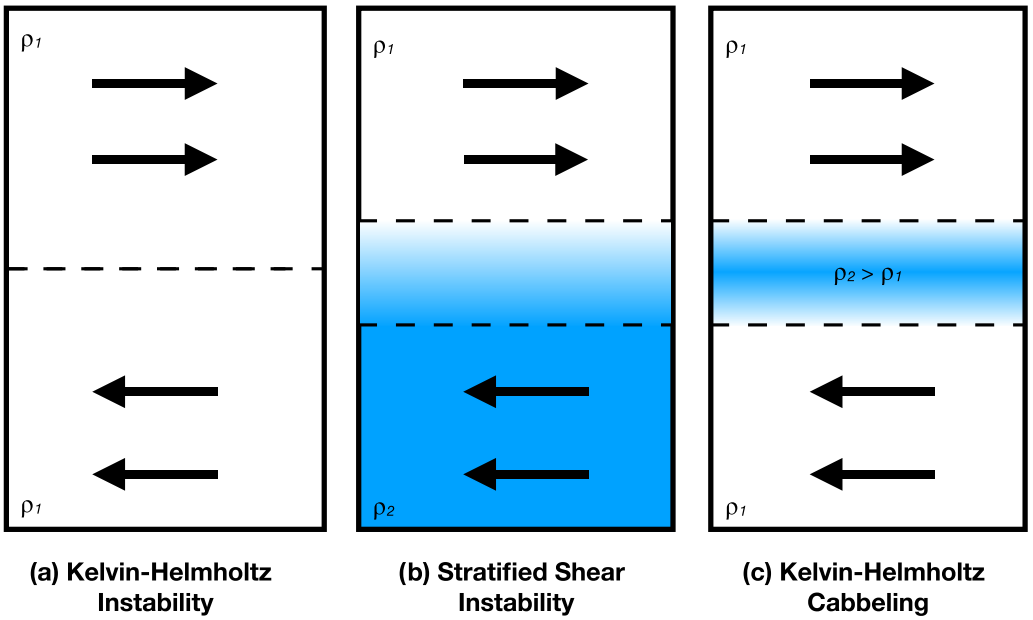

FIG. 2. Schematic representation of the background state for (a) unstratified KH instabilities, (b) stratified shear instabilities, and (c) stratified shear instabilities in the cabbeling regime. Note that the classical RT instability is represented in panel (c) without the arrows.

ocean is found to be highly patchy over all regions but the Southern Ocean (see Fig. 4 in [12]). A different point of view on the role of cabbeling in large-scale motions is provided by the theoretical study of Thomas and Shakespeare [21], who developed a model for the effects of cabbeling during frontogenesis, which they then simplify using perturbation methods and apply for parameters relevant to the Gulf Stream. The detailed fluid mechanics of how cabbeling takes place is outside of the realm of the model by construction.

In what follows, we consider a shear layer that is temperature stratified, and the temperature stratification spans T^*. This implies that embedded in the shear layer is a thin, statically unstable layer, which in the absence of shear would yield a Rayleigh-Taylor instability [13]. If we considered only the shear layer, the relevant instability would be the Kelvin-Helmholtz instability, shown in Fig. 2(a). The typical stably stratified shear layer is shown in Fig. 2(b). Our situation is schematized in Fig. 2(c), which shows that we have a hybrid of the Rayleigh-Taylor (henceforth RT) and Kelvin-Helmholtz (henceforth KH) instabilities. While the KH instability has a clear preferential direction aligned with the shear flow, the RT instability is isotropic in the horizontal plane. Yet in the cabbeling regime the buoyancy effects are weak, and hence a basic research question concerns the extent to which the onset of instability is three-dimensional (3D).

RT instability in the presence of shear has been studied both experimentally [22] and via simulations [23]. Akula *et al.* [22] use a splitter plate in a gas tunnel to generate a spatially growing RT instability with shear. Their Reynolds numbers range from around 30 000 to 110 000, with velocities on the order of 0.7 m s^{-1}. Reported Atwood numbers range from 0.035 to 0.159. Both of these will turn out to be in a significantly different part of parameter space from the simulations we report. Nevertheless, the authors report a transition from shear-dominated to buoyancy-dominated flow, a theme that will be taken up in our simulations, reported below. Olson *et al.* [23] use an immiscible fluid model to simulate shear influenced RT instability. Their Reynolds number, while lower than that in the experiments of Akula *et al.* [22], is in the thousands. They present comparisons of direct numerical simulations and large eddy simulations (LESs), finding that sufficiently resolved

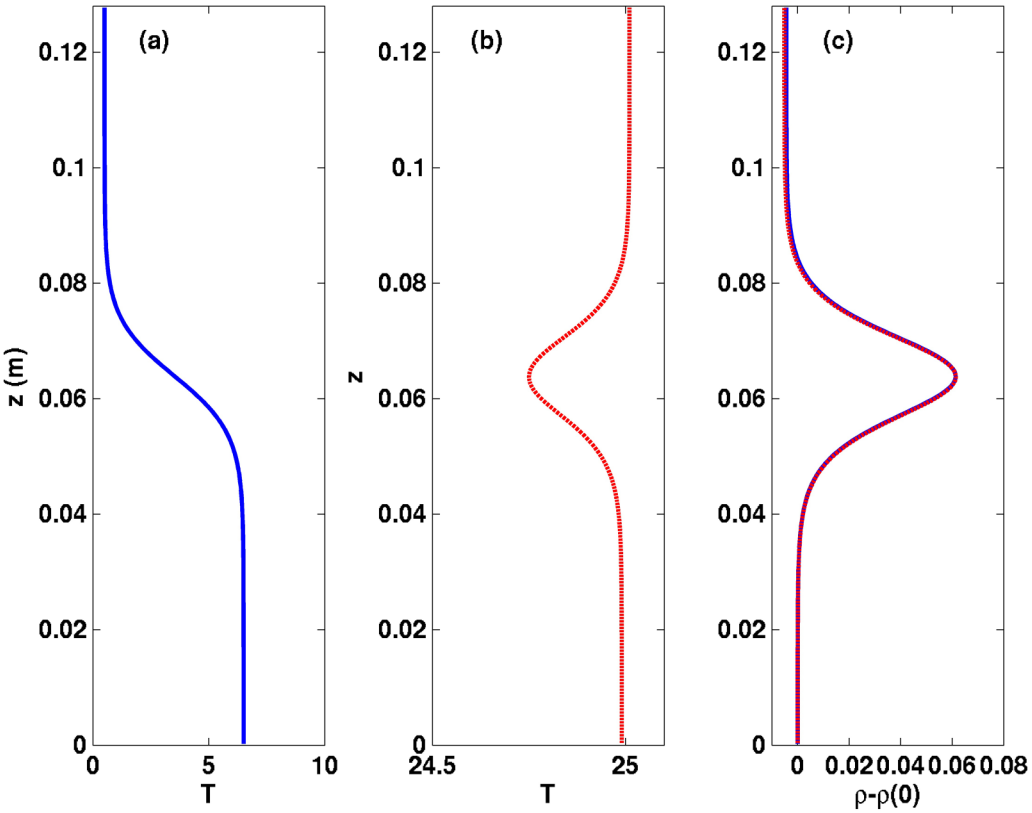

FIG. 3. Temperature profiles corresponding to regions of interest as presented in Fig. 1. The leftmost plot considers cold water, which is susceptible to cabbeling, while the middle is concerned with water at higher temperatures. The latter temperature regime was chosen such that both cases would have the same density profile, as shown in the rightmost panel.

LESs represent growth of the mixing interface quite well. The authors also document the transition from RT to KH instability as the shear strengthens (their Fig. 14 [23]). However their typical Atwood numbers are larger than 0.1, meaning that like those of Akula *et al.* [22], their results pertain to a different region of parameter space than that which we set out to explore.

A second, fundamental research question is whether cabbeling itself affects the evolution of the mature instability. As shown in Fig. 1, it is possible to construct a direct analog of a given density profile, $\bar{\rho}(z)$, from the cabbeling regime using warm water. We show an example in Fig. 3. While the onset of instability can be expected to be nearly identical for the cabbeling [Fig. 3(a)] and noncabbeling [Fig. 3(b)] cases, it is unknown how closely the two cases will track as the instabilities reach a fully three-dimensionalized state. Indeed, the two cases are not formally dynamically equivalent since both evolve temperature and diagnose density, meaning that the nonmonotonicity of the equation of state in cold water is relevant only to the cabbeling case. Nevertheless, direct examination of the results indicates that the early stages of evolution are very similar. As an aside, we do not refer to this state as "turbulent" due to the low Reynolds number.

The remainder of this paper is organized as follows: the Methods section presents the governing equations, briefly discusses the numerical model used as well as the relevant dimensionless parameters, and concludes with a linear hydrodynamic stability analysis. The subsequent Results section begins by comparing 2D and 3D simulations focusing on the onset of the instability. This is followed by a comparison of the cabbeling and noncabbeling results, where variations of the strength of the

initial shear are explored in both regimes. The Results section is concluded by discussing the major differences between the mechanisms at work, namely, buoyancy and shear. The final section of the paper discusses the primary conclusions and identifies directions for future work.

II. METHODS

A. Governing equations and numerical methods

In the context of early spring-time, temperate lakes, the stratified Navier-Stokes equations under the Boussinesq approximation are the relevant set of governing equations. However, most literature on simulating lakes makes at least some simplifications (commonly, the hydrostatic assumption). We will retain the full equations since we will consider a very small portion of a lake. In our context, temperature differences in the domain are small (typically less than 3 °C), implying that density differences will be extremely small as well. For an initial state that remains below the temperature of maximum density, a typical density difference is 0.15 kg m^{-3}. If we define the Atwood number as in the Introduction, we get a value of 3.3×10^{-5}. Thus, while buoyancy remains a vital term in the equations, its effects are anticipated to be small. The governing equations under the Boussinesq approximation with reference density, ρ_0, [24] read

$$\vec{\nabla} \cdot \vec{u} = 0, \tag{1}$$

$$\frac{D\vec{u}}{Dt} = -\frac{1}{\rho_0}\vec{\nabla} p + \nu \nabla^2 \vec{u} - \frac{\rho(T)}{\rho_0} g\hat{k}, \tag{2}$$

$$\frac{DT}{Dt} = \kappa \nabla^2 T, \tag{3}$$

where $\frac{D}{Dt}$ is the material derivative, $\vec{u} = (u, v, w)$ is the fluid velocity, p is the pressure, ρ is the density, ν is the kinematic viscosity, κ is the thermal diffusivity, T is the temperature, and g is the acceleration due to gravity. Here $\rho(T)$ is the equation of state specified according to Brydon *et al.* [25]. The effects of solar radiation, while important at the field scale, are ignored for our process studies.

Simulations were performed with the pseudospectral code SPINS [26], in its DNS configuration. The domain was rectangular in shape, with $(L_x, L_y, L_z) = (0.256, 0.064, 0.128)$ m, and grid of $(N_x, N_y, N_z) = (512, 128, 256)$ points, implying a resolution of 0.5 mm in all three directions. The channel was periodic in the L_x, or along channel, and L_y, or spanwise, directions, and free slip (no flux) boundary conditions were applied at $z = 0, L_z$ to the velocity (temperature) field. The 2D simulations (which were performed first) were configured with $(L_x, L_z) = (0.512, 0.128)$ m, and a grid of $(N_x, N_z) = (2048, 256)$, resulting in a higher resolution (0.25 mm) in the x-direction, as compared to the z-direction (0.5 mm). Note that both L_y and N_y are equal to one in this case. Grid halving studies suggested all results reported are insensitive to grid refinement. Both preliminary simulations and linear stability calculations suggest that the domain length chosen is large enough to fully resolve the dominant instability. Since the majority of simulations discussed below are 3D, only when 2D simulations are discussed will cases have "2D" appended to their case acronym (see Tables I and II for Case Labels).

It is worth commenting further on resolution. The instabilities we explore never reach a truly turbulent state, and hence scaling based on Kolmogorov and Batchelor scales is not expected to apply to the results we report. Our grid resolution of 0.5 mm was sufficient to resolve gradients of temperature and velocity components. One-dimensional (1D) spectra, including those of the temperature gradient (not shown in the figures), showed no evidence of spectral blocking. A quantitative study of the fully turbulent state, especially one focusing on local isotropy or dissipation mechanisms, should likely adopt an even finer grid than the one we used, and the definition of a relevant dissipation and mixing scale should be re-evaluated at that time.

TABLE I. Cases considered, including case label and their dimensional parameters. Cases with an asterisk indicate cases presented in both two and three and dimensions (all others are 3D only).

Label	Description	Δu (m s^{-1})	T_0 °C	ΔT °C
CB*	Basic Cabbeling Shear Instability	0.01	2	4
CBH	Weaker Cabbeling Shear Instability	0.005	2	4
CBD	Stronger Cabbeling Shear Instability	0.02	2	4
F	Basic No Cabbeling Shear Instability	0.01	25	1
FH	Weaker No Cabbeling Shear Instability	0.005	25	1
FD	Stronger No Cabbeling Shear Instability	0.02	25	1
RT*	Rayleigh-Taylor Instability (No shear)	0	2	4
KH*	Kelvin Helmholtz Instability (No buoyancy)	0.01	N/A	N/A

B. Derived diagnostic quantities

Following standard practice, the kinetic energy density is defined without the factor of ρ_0 as

$$ke(x, y, z, t) = \frac{1}{2}(u^2 + v^2 + w^2). \tag{4}$$

Since the streamwise velocity component u is the only component with an initial velocity we define

$$U(z, t) = \frac{1}{L_x L_y} \int_0^{L_x} \int_0^{L_y} u(x, y, z, t)\, dx\, dy. \tag{5}$$

We can then define a kinetic energy based on this "background" velocity

$$ke_{u_b} = \frac{1}{2} U(z, t)^2 \tag{6}$$

as well as three components of kinetic energy which we expect, *a priori*, to be of comparable magnitude during the evolution of the instability:

$$ke_{u_p} = \frac{1}{2}(u - U)^2, \quad ke_v = \frac{1}{2} v^2, \quad ke_w = \frac{1}{2} w^2. \tag{7}$$

TABLE II. Cases considered, including case label, a short description, dimensionless numbers, and a list of figures in which they appear. Cases with an asterisk indicate cases presented in both two and three and dimensions (all others are 3D only).

Label	Description	Re	Fr_v	Pe	Figures
CB*	Basic Cabbeling Shear Instability	100	3.94	704	All
CBH	Weaker Cabbeling Shear Instability	50	1.97	352	4, 15, 16, 17
CBD	Stronger Cabbeling Shear Instability	200	7.88	1408	4, 15, 16, 17, 18
F	Basic No Cabbeling Shear Instability	100	3.94	704	1, 3, 12, 13, 14, 15, 17, 18
FH	Weaker No Cabbeling Shear Instability	50	1.97	352	15, 17
FD	Stronger No Cabbeling Shear Instability	200	7.88	1408	15, 17
RT*	Rayleigh-Taylor Instability (No shear)	N/A	N/A	N/A	2, 4, 5, 10, 17, 18
KH*	Kelvin Helmholtz Instability (No buoyancy)	100	N/A	704	2, 4, 5

These components can then be integrated to give mean quantities that describe the energetics of the instability evolution:

$$KE_{u_b}(t) = \int_0^{L_x}\int_0^{L_y}\int_0^{L_z} ke_{u_b}\,dx\,dy\,dz, \tag{8}$$

$$KE_{u_p}(t) = \int_0^{L_x}\int_0^{L_y}\int_0^{L_z} ke_{u_p}\,dx\,dy\,dz, \tag{9}$$

$$KE_{v}(t) = \int_0^{L_x}\int_0^{L_y}\int_0^{L_z} ke_{v}\,dx\,dy\,dz, \tag{10}$$

$$KE_{w}(t) = \int_0^{L_x}\int_0^{L_y}\int_0^{L_z} ke_{w}\,dx\,dy\,dz. \tag{11}$$

The above decomposition is similar to a decomposition used in studies of stably stratified KH and Holmboe instabilities (e.g., [8]). However, in situations where Squire's theorem is expected to apply, the decomposition consists of several steps: first, separate the velocity field into a part that has only a vertical and temporal variation (i.e., the 1D part), a part that has only a dependence in the x-z directions (this is often labeled as "2D"), and a part that is the velocity component minus the 1D and 2D parts (this is often labeled as "3D"). The fact that the RT instability is horizontally isotropic led us to avoid the second and third steps in the decomposition.

The efficiency of the cabbeling process can be tracked by considering the volumetric fraction occupied by fluid within a fixed percentage of the initial density change, $\Delta\rho = \max[\rho(t=0)] - \min[\rho(t=0)]$, of the maximum possible density, $\rho_{\max}$. If $H(\cdot)$ represents the indicator, or Heaviside step function, we let

$$CB_{10}(t) = \frac{1}{L_xL_yL_z}\int_0^{L_x}\int_0^{L_y}\int_0^{L_z} H[\rho - (\rho_{\max} - 0.9\Delta\rho)]\,dx\,dy\,dz, \tag{12}$$

$$CB_{1}(t) = \frac{1}{L_xL_y}L_z\int_0^{L_x}\int_0^{L_y}\int_0^{L_z} H[\rho - (\rho_{\max} - 0.99\Delta\rho)]\,dx\,dy\,dz. \tag{13}$$

In order to discuss the evolution of the instability as a function of time and height we let

$$\langle cb_{10}\rangle_{xy}(z,t) = \frac{1}{L_xL_y}\int_0^{L_x}\int_0^{L_y} H[\rho - (\rho_{\max} - 0.9\Delta\rho)]\,dx\,dy, \tag{14}$$

$$\langle cb_{1}\rangle_{xy}(z,t) = \frac{1}{L_xL_y}\int_0^{L_x}\int_0^{L_y} H[\rho - (\rho_{\max} - 0.99\Delta\rho)]\,dx\,dy, \tag{15}$$

$$\langle T\rangle_{xy}(z,t) = \frac{1}{L_xL_y}\int_0^{L_x}\int_0^{L_y} T(x,y,z,t)\,dx\,dy. \tag{16}$$

The first two quantities allow for the tracking of where the densest fluid is located in the water column at two different thresholds; the third tracks the vertical distribution of temperature. This last quantity is important because the temperature, and not the density, is the quantity evolved by the numerical model. Horizontal averages of the components of kinetic energy would be defined in an identical manner to the temperature, while spanwise averaged quantities are defined analogously to the above. For example, the spanwise average of the density would be $\langle\rho\rangle_y$.

C. Initialization, dimensionless parameters, and experimental design

All simulations are initialized from a horizontal shear flow

$$U(z) = \frac{\Delta u}{2}\tanh\left(\frac{z - L_z/2}{L_{\text{shear}}}\right). \tag{17}$$

Cases with cabbeling used a similar form for the temperature field,

$$T(z) = T_0 + \frac{\Delta T}{2}\left[1 + \tanh\left(\frac{z - L_z/2}{L_{\text{temp}}}\right)\right]. \tag{18}$$

T_0 and ΔT were chosen so that the temperature field extends the same number of degrees above and below the temperature of maximum density. The initial density field is thus weakly statically unstable, since the temperature of maximum density occurs near the domain middepth. Cases without cabbeling, or the cases we label as "fit," used a more complex form for the initial temperature,

$$T(z) = T_0 - \frac{\Delta T}{4}\text{sech}^2\left(\frac{z - L_z/2}{L_{\text{temp}}}\right) + 0.01\tanh\left(\frac{z - L_z/2}{L_{\text{temp}}}\right). \tag{19}$$

The first term of this equation sets the reference temperature, the second sets the unstable density profile (needed because T_0 is chosen to be well above the temperature that yields a maximum density), while the third term corrects so that the "fit" density profile matches the initial density profile in the cabbeling cases. Parameter values, along with the labels of the cases discussed below are given in Table I. The range of temperatures for the cabbeling cases are chosen as typical of spring time conditions. Δu is the parameter varied in order to change the initial shear. Its value is uncertain, though our choices are more or less representative of observations [15] and recent simulations [19]. While it is also possible to vary the initial shear by varying, L_{shear}, we consider initial shear strength and initial current strength as synonymous. As we will demonstrate below, the initial evolution is dominated by the velocity shear as opposed to the buoyancy. Moreover, the vertical length scale, L_{temp}, set by the thickness of the initially unstable layer, is a quantity that is important to the dynamics but with no observational constraints at the time of writing, was selected in an *ad hoc* manner, setting $L_{\text{temp}} = L_{\text{shear}}$.

A natural length scale for the problem is given by the vertical scale of the shear layer, $L = L_{\text{shear}}$. Similarly, this parameter is not strongly observationally constrained, though based on Ulloa *et al.* [19], $L_{\text{shear}} \sim 0.01$ m, is a reasonable choice. A natural velocity scale is given by the velocity difference across the shear layer, hence $U = \Delta u \sim 0.01\ \text{ms}^{-1}$ for the base cases CB and F in Tables I and II. The timescale is then set to equal the advective timescale, $t_{\text{advective}} = L/U$, and the pressure is scaled by the dynamic pressure, $\rho_0 U^2$. With these parameters given, the governing equations can then be nondimensionalized in terms of the three standard dimensionless parameters, the Reynolds (Re), Péclet (Pe), and Froude (Fr) numbers:

$$\vec{\nabla}\cdot\vec{u} = 0, \tag{20}$$

$$\frac{D\vec{u}}{Dt} = -\vec{\nabla}p + \frac{1}{\text{Re}}\nabla^2\vec{u} - \frac{1}{\text{Fr}^2}R(T)\hat{k}, \tag{21}$$

$$\frac{DT}{Dt} = \frac{1}{\text{Pe}}\nabla^2 T. \tag{22}$$

Here $R(T)$ is the dimensionless form of the equation of state of Brydon *et al.* [25], and the dimensionless numbers are specified in terms of the problem parameters and physical constants as

$$\text{Re} = \frac{UL}{\nu}, \tag{23}$$

$$\text{Fr} = \frac{U}{\sqrt{gL}}, \tag{24}$$

$$\text{Pe} = \frac{UL}{\kappa}, \tag{25}$$

$$\text{At} = \frac{\rho_{\max} - \rho_{\min}}{2\rho_0}, \tag{26}$$

where Re gives the ratio of inertia to viscous terms, Fr gives the ratio of the buoyancy term to the inertia terms, and Pe gives the ratio between the nonlinear and diffusion terms in the temperature equation. The Grashof number, Gr, gives the ratio between buoyancy and viscous terms and is estimated as $\mathrm{Gr} \approx 10^5$. Since the stratification is temperature controlled the Prandtl number is held fixed at $\mathrm{Pr} = 7$. Scaling thus suggests the flow is transitional, low Froude number, with diffusive and viscous effects largely negligible compared to buoyancy effects. While the gradient Richardson number, $\mathrm{Ri} = N^2/U_z^2$, is often used to discuss stratified shear instability [20], for the cabbeling regime, the initially unstable stratification would imply $\mathrm{Ri} < 0$ for a portion of the water column, and hence that classical results based on Ri provide little insight. However, it is useful to define a more dynamically relevant Froude number that includes the density differences inherently present in the system. This is the vertical Froude number, defined as $\mathrm{Fr}_v = \mathrm{Fr}/\sqrt{2\mathrm{At}}$, using the definition of the Atwood number, At, as given above. This modified dimensionless number is better able to show that buoyancy effects are weak, as expected. Estimated values of dimensionless parameters are given for the various cases discussed below in Table II. Table II also provides a list of figures that give detailed information about the various cases.

The cases summarized in Tables I and II were designed to test how changes in Reynolds number influence the 3D evolution of the cabbeling shear instability. The cases marked "F" were initialized with a warm water temperature profile, for which cabbeling is impossible. The initial temperature profile was chosen so that the resulting density profile matched that in the "CB" cases. This allows us to compare and contrast three-dimensionalization with and without cabbeling. The other two cases were chosen to correspond to classical instabilities and provide context for the "CB" cases.

D. Stability analysis

The classical linear theory of the hydrodynamic stability of a stratified shear flow yields the Taylor-Goldstein (henceforth T-G) equation for the complex phase velocity, $c = c_R + ic_I$, and the vertical structure, $\phi(z)$, of the perturbation stream function, ψ,

$$[U(z) - c]\left(\frac{d^2}{dz^2} - k^2\right)\phi - U_{zz}\phi + \frac{N^2(z)}{U - c}\phi = 0 \tag{27}$$

with the boundary conditions $\phi(0) = \phi(L_z) = 0$. This theory is inviscid and hence may not be appropriate for the low Reynolds number regime discussed in this paper. The theory has been extended to include viscous and diffusive effects, with an accompanying open source solver available for download [27]. The governing equations are now more complicated, with a fourth-order ODE governing perturbations of the vertical component of velocity, $\hat{w}$, and a second-order ODE governing density perturbations, $\hat{\rho}$:

$$\sigma\nabla^2\hat{w} = -ikU\nabla^2\hat{w} + ikU_{zz}\hat{w} + \nu\nabla^4\hat{w} - \frac{g}{\rho_0}k^2\hat{\rho}, \tag{28}$$

$$\sigma\hat{\rho} = -\hat{w}\bar{\rho}_z - ikU\hat{\rho} + \kappa\nabla^2\hat{\rho}, \tag{29}$$

where σ is the complex frequency, and $\bar{\rho}(z)$ is the background density profile. This problem is converted to a generalized eigenvalue problem with a block structure (see [27] for details).

We applied a pseudospectral technique based on Chebyshev polynomials, following the book by Trefethen [28] to solve the T-G equation and the open source code of Lian *et al.* [27] to solve the viscous problem.

III. RESULTS

When the vertical temperature profile spans T^*, the temperature of maximum density, shear flow may be susceptible to both shear and Rayleigh-Taylor instability. In Fig. 4 we show growth rate profiles as a function of the wave number, k, computed using the viscous/diffusive version of the T-G equation (28) and (29) as implemented in [27]. In the upper panel, the density profile is held

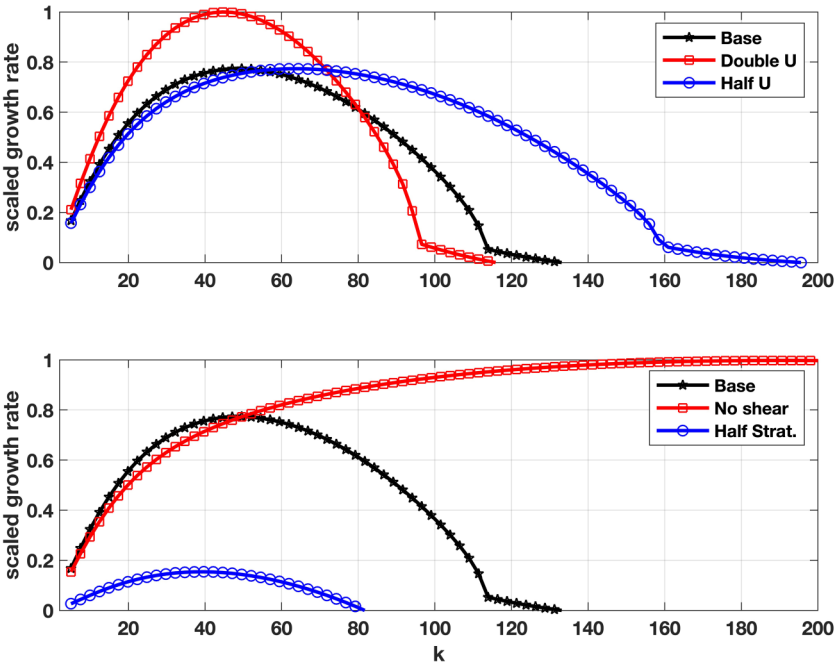

FIG. 4. The normalized growth rate in the viscous/diffusive linear stability theory for a variety of stratification and velocity profiles. In the upper panel, the density profile is held fixed while the strength of the background shear is varied. Doubling the shear increases the growth rate by roughly 20% but does not change the wave number of fastest growth to any significant degree. Halving the shear does not change the maximum growth rate, but shifts the wave number to larger k and broadens the growth rate curve. In the bottom panel, a case without shear (red) and with a weaker unstable stratification (blue) are shown. The case without shear exhibits a monotonically increasing growth rate as a function of k. The case with the weaker unstable stratification has a maximum growth rate reduced by about a factor of four from that observed in the base case.

fixed while the strength of the background shear is varied. Doubling the shear increases the growth rate by roughly 20% but does not change the wave number of fastest growth to any significant degree. Halving the shear does not change the maximum growth rate, but shifts the wave number to larger k and broadens the growth rate versus wave number curve. The wave number at which the peak growth rate is observed corresponds to length scales that are, at worst, about half of the streamwise extent of the simulations. In the bottom panel, the base case is accompanied by the case without shear (red) which exhibits a monotonically increasing growth rate as a function of k. The case with a stratification reduced by 50% is shown in blue. It can be seen that the critical wave number does not change a great deal, but the growth rate is reduced by a factor of four. Comparisons with solutions of the T-G equation (not shown) suggest that the dominant effects of viscosity and diffusivity are for values of $k > 100$. It is worth noting that compared to published results for the stably stratified KH instability (see, for example, the classical paper by Hazel [1]), the unstable stratification in our study leads to a shift to larger k (shorter perturbations). Nevertheless, since the unstable stratification is weak, the finite amplitude manifestation of shear instability is expected to involve billows, with perturbation vorticity oriented in the spanwise direction that begins as nearly 2D. In contrast, a shear-free RT instability is isotropic in the horizontal plane. For this reason, we present both 2D and 3D simulations, with a focus on the latter.

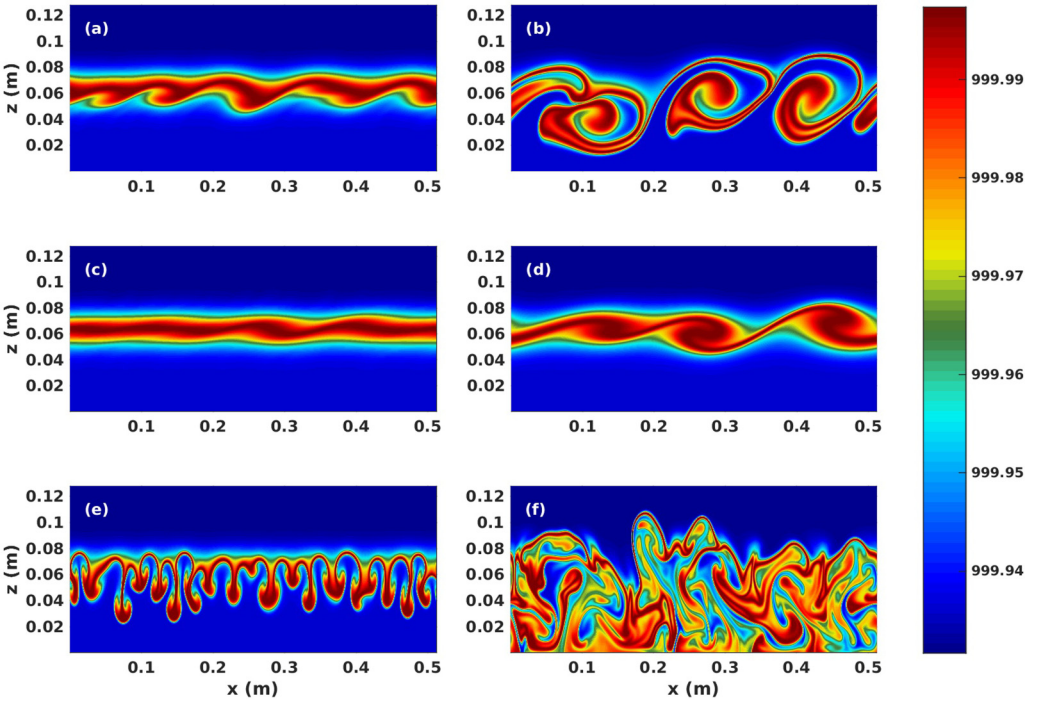

FIG. 5. Onset and development of instability as expressed in the density field at $t = 50$ s (left column) and $t = 100$ s (right column). Panels (a) and (b) represent cabbeling shear flow (case CB2D), (c) and (d) the pure KH instability (case KH2D) for which the density is a passive tracer (i.e., $g = 0$), whereas (e) and (f) depict the RT instability (case RT2D).

A. Evolution in two dimensions

We compare a stratified shear instability in the cabbeling regime (case CB2D) to both the unstratified KH instability (case KH2D), which involves a background shear flow but no density stratification, as well as the standard RT instability (case RT2D), in which there is an unstable density stratification but no shear flow. The nature by which these instabilities lead to mixing depends largely on the driving forces involved, either shear or buoyancy. In the cabbeling regime, an initial temperature profile with temperatures that lie both above and below the temperature at which maximum density occurs results in an initial density field that is weakly statically unstable (located along the domain middepth). The combination of a velocity shear alongside the existence of this dense midwater column region ultimately leads to a competition between sinking and the formation of billows.

Figure 5 compares and contrasts the cabbeling shear instability (case CB2D) with unstratified KH instability (KH2D) and shear-free RT instability (RT2D) at $t = 50$ s [Figs. 5(a), 5(c), and 5(e)] and $t = 100$ s [Figs. 5(b), 5(d), and 5(f)]. The initial stages of the cabbeling instability are dominated by shear as evidenced in Figs. 5(a) and 5(c), which track much more closely than Figs. 5(a) and 5(e), where the latter shows the RT instability. As the instability begins to develop further, we start to see the effects of buoyancy in Fig. 5(b). The form of the instability in Fig. 5(b) visually differs from the KH instability shown in Fig. 5(d). Though not as chaotic in nature as the RT instability in Fig. 5(f), the shear instability in the cabbeling regime begins to display billow-like formations which are systematically shifted so that their centers lie below the domain middepth. This hints that the effects of buoyancy in the cabbeling regime will become most important at later times, or rather, the unique aspects of shear instability in the cabbeling regime will be most evident when the

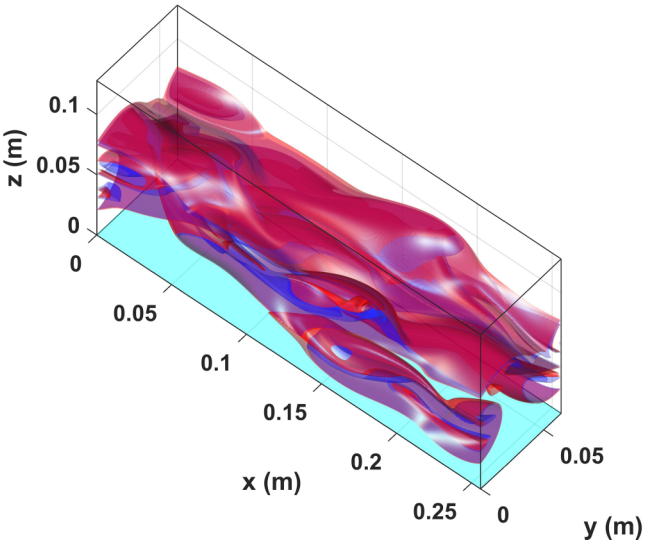

FIG. 6. Isosurface plot of the density at $t = 75$ s for case CB. The red, less transparent surface, corresponds to density values that are 10% above the midpoint of the density range, whereas the dark blue surface represents density values that are 10% below the density midrange. For illustrative purposes, the bottom of the tank has been shaded teal. The effect of cabbeling shifts the center of activity in the instability down from the center of the shear layer.

instability has time to develop to a finite amplitude regime. For these times, we expect 3D effects will be dominant. A particular issue to explore is that a shear-free RT instability does not have a preferred wave number direction in the horizontal plane. This means that while the KH instability has well-studied routes (i.e., secondary instabilities) to a fully three-dimensionalized state [2,3], the cabbeling regime may not adhere to these.

B. Three-dimensionalization

We illustrate the effects of three-dimensionalization in the cabbeling regime by first examining a series of isosurface plots, which represent surfaces of constant density within the confines of the tank for case CB. Three-dimensionalization occurs through RT-like secondary instabilities. Cabbeling efficiency, as expressed in quantities like $CB_{10}(t)$ and $CB_1(t)$ [Eqs. (12) and (13)], is expected to increase in the fully three-dimensionalized state, as a result of enhanced mixing due to 3D motions (see detailed discussion below). Cabbeling is efficient as a result of mixing, yet it in itself acts as a feedback mechanism to increase this mixing by producing denser fluid.

Figures 6–9 highlight isosurfaces with density values that are 10% above and below the midpoint of the density range. The specific values used were chosen by trial and error to make the 3D images visually appealing. In the cabbeling regime, the value of maximum density occurs along the domain middepth at the beginning of the simulation but transitions to the lower half of the domain when the effects of buoyancy begin to play a more prominent role. In Figs. 6 and 7, we see a snapshot of the simulation at $t = 75$ s, with a focus on the top and bottom views of the tank, respectively, whereas Figs. 8 and 9 correspond to an output time of $t = 100$ s. We include both orientations to highlight the vertical asymmetry introduced by cabbeling effects. As previously noted, the effects of an unstable density distribution on shear instability (i.e., cabbeling in the present context) work to shift the activity of the instability to the lower half of the domain. Hence, we see a higher proportion of dense fluid near the bottom of the tank where an increasingly complex isosurface at later times (specifically $t = 100$ s) indicates that the effects of three-dimensionalization are dominant. This is

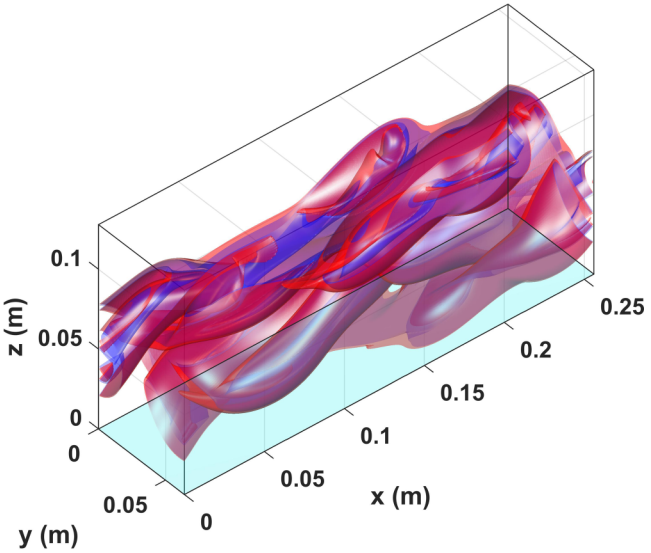

FIG. 7. Dynamics as in Fig. 6 now viewed from the bottom. More high-density fluid is visible in this orientation. The activity of the instability is predominantly in the lower half of the domain.

despite the low Reynolds number of the simulation. Indeed, the contrast with the typical horizontally averaged profiles for stratified KH and Holmboe instabilities shown in Salehipour *et al.* [8] (their Fig. 12 [8]) is profound.

Figure 10 shows a plot of the kinetic energy components for case CB, scaled by the initial nonzero component of the kinetic energy based on the background shear flow. This component, KE_{u_b}, is included in Fig. 10(a) to highlight the substantial difference between it and the more

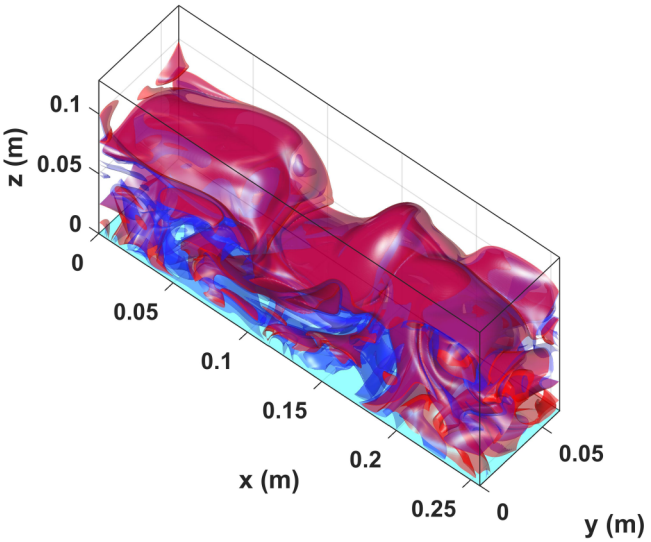

FIG. 8. Isosurface plot of the density at $t = 100$ s for case CB. The corresponding density values of the red and blue isosurfaces are the same as those stated in Fig. 6. The center of activity in the instability remains shifted downwards at later times, while the degree of three-dimensionalization has significantly increased.

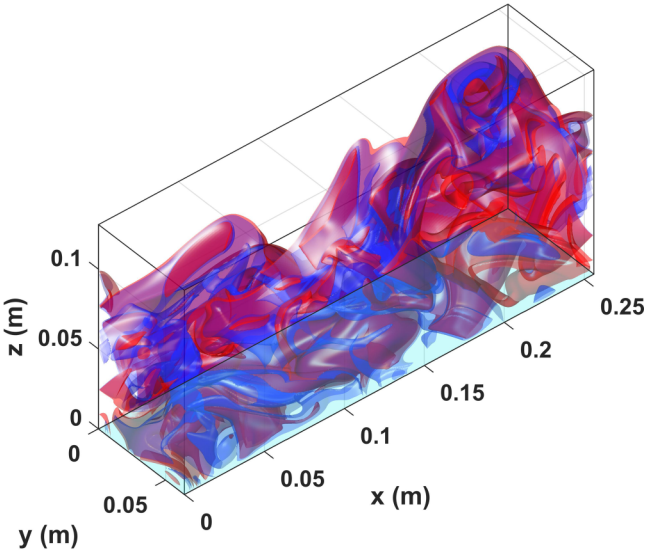

FIG. 9. Corresponding view of Fig. 8 from the bottom of the tank. A more complex representation of the isosurface can be seen at this later time and, more specifically, at this angle.

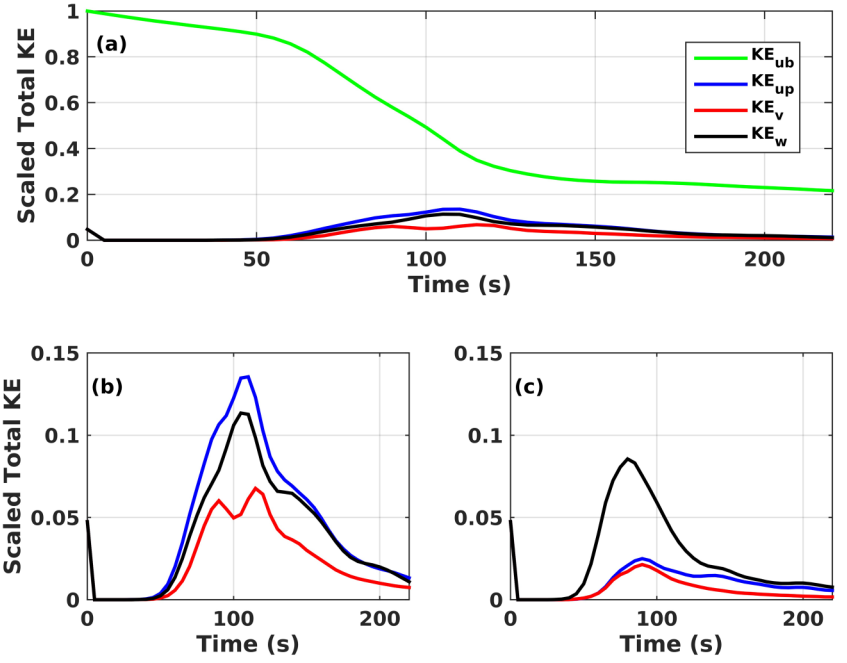

FIG. 10. (a) Plot of the kinetic energy components for case CB scaled by $KE_{u_b}(0)$, with colors corresponding to KE_{u_b} (green) KE_{u_p} (blue), KE_v (red), and KE_w (black), respectively. (b) Detail of the three perturbation kinetic energy components for the case CB. (c) Detail of the three perturbation kinetic energy components for the case RT.

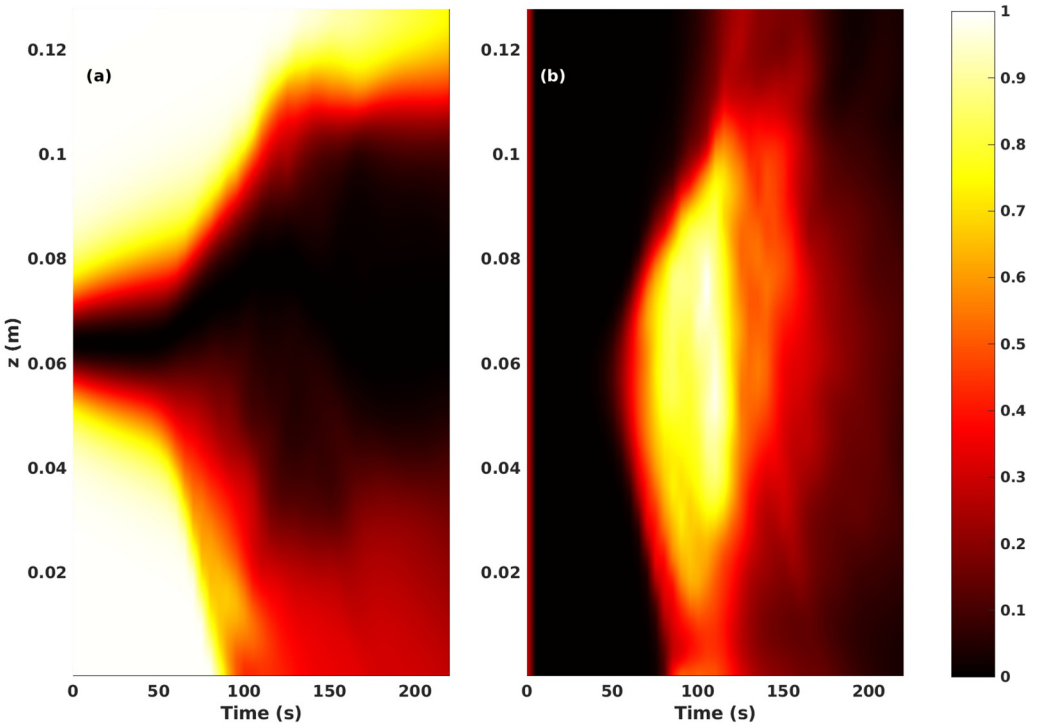

FIG. 11. (a) The horizontally averaged background kinetic energy, $\langle ke_{u_b} \rangle_{xy}(z,t)$, for case CB, scaled by its maximum value as a function of z and t. (b) The horizontal average of the perturbation kinetic energy $\langle ke_{u_p} + ke_v + ke_w \rangle_{xy}(z,t)$, for case CB, scaled by its maximum values as a function of z and t.

comparable perturbation quantities. Figure 10(b) provides a more detailed view of the perturbation kinetic energy components, where we can see that the energy associated with KE_{u_p} is greatest for the duration of the simulation followed closely by KE_w, and finally, KE_v. All components reach their respective peaks around $t = 100$ s, at which point the instability is in a fully three-dimensionalized state. We are able to compare the energetics of the cabbeling instability to the more common RT instability by considering Fig. Figure 10(c), which shows the details of the three perturbation kinetic energy components for the latter case. The main difference between the two instability types is in the division of energy among components. For the RT instability, the energy associated with KE_w is significantly larger than either of the spanwise or streamwise components. These remaining components are of comparable size, as can be expected given that a shear-free RT instability is isotropic in the horizontal plane. Overall, the energy associated with the RT instability is smaller than in the cabbeling case as evidenced by comparing the vertical scale of the individual components between panels.

If we consider the horizontally averaged kinetic energy, we gain insight into the distribution of the kinetic energy with z and time. Figure 11 shows $\langle ke_{u_b} \rangle_{xy}$ [Fig. 11(a)] and $\langle ke_{u_p} + ke_v + ke_w \rangle_{xy}$ [Fig. 11(b)]. Since the purpose of this figure is to outline the spatiotemporal pattern of the two quantities, these have been scaled by their maximum values such that the colorbar ranges between zero and one. We see in Fig. 11(a) that up to $t = 70$ s, the horizontal background current is only slightly smeared by viscosity. The fluid near the middle of the domain, which is the most dense (see Fig. 12 for further clarification), moves quite slowly. As the instability sets in, the region in which the background kinetic energy is low spreads in the z direction. In Fig. 11(b) we exclude the background flow effects, and see that around $t = 100$ s there is a significant burst of activity. The region of activity rapidly spreads in the vertical, decreasing in intensity as it does so. Activity is

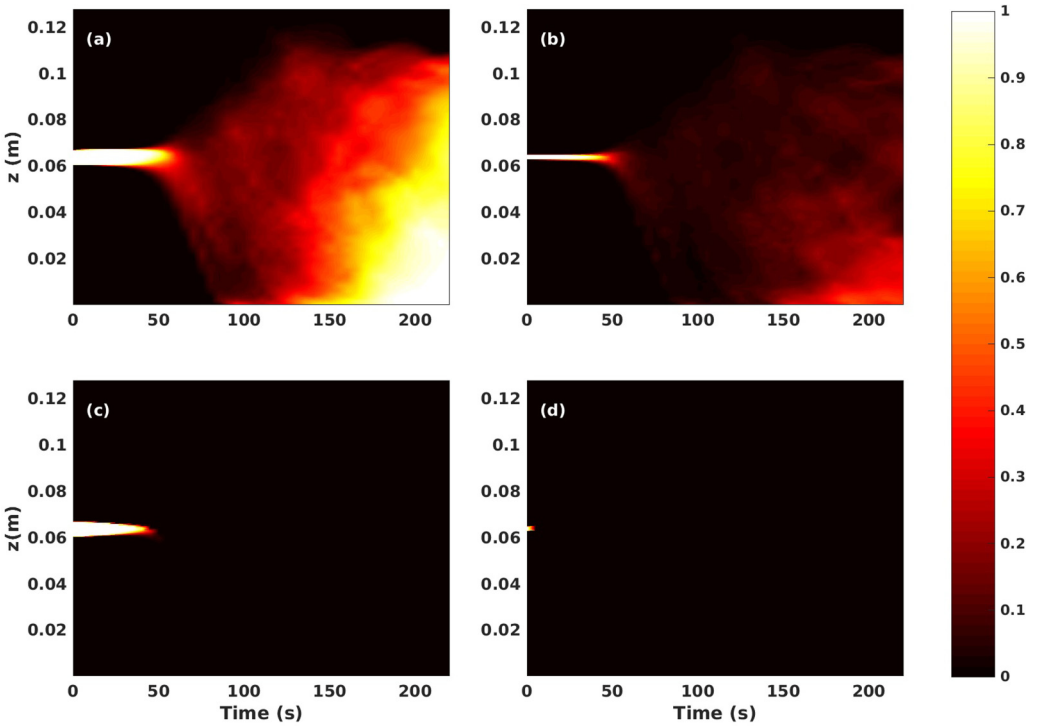

FIG. 12. The fraction of fluid within 10% of the maximum density, $cb_{10}(z,t)$, as a function of z and t, for (a) case CB and (c) case F. The fraction of fluid within 1% of the maximum density, $cb_1(z,t)$, as a function of z and t, for (b) case CB and (d) case F.

centered below the middepth, excludes a thin region above $z = 0.11$ m, and weakens (but does not disappear) near the bottom boundary. By late times, $t > 180$ s, perturbation motions are relatively small over the entire water column. Returning to Fig. 11(a), we note that at these later times (after $t = 180$ s), the fully three-dimensionalized instability has separated the domain into three distinct regions: a thin upper region of the tank which hosts faster moving fluid, a broad, slowest-moving middle region, and a near bottom region which is slowed from its initial speed, but remains faster moving than the central region. Thus, the instability does not lead to a complete homogenization of velocity.

In order to put the above observations into context we next turn to an intercomparison of the cases with cabbeling to those without it. This will be accomplished by contrasting case CB with an initial state that has the same density profile, but a temperature well outside of the cabbeling regime (case F). An illustration of the corresponding density profile, both within and well outside of the cabbeling regime, is shown in Fig. 1. In each instance, the initial streamwise velocity profile was identical, and the same small white noise perturbation was used to trigger the instability. The temperature differences, however, are set by the equation of state since we choose to match the initial density (not temperature) profile.

C. Cabbeling versus no cabbeling cases and variations in Reynolds number

As mentioned above, the ability to produce dense fluid, or cabbeling efficiency, is expected to increase in the fully three-dimensionalized state, or after approximately $t = 100$ s. Figure 12 shows the vertical distribution of the volume of fluid within 10%, $\langle cb_{10}\rangle_{xy}$, and 1%, $\langle cb_1\rangle_{xy}$, of the density maximum for cases CB and F. If we look at the fraction of fluid within 10% of the maximum density

[Figs. 12(a) and 12(c)], we see that this fluid is concentrated near the middle of the domain at the beginning of the simulation for both cases. While the density matches between the two cases, the temperature differences for case F are much smaller (this is set by the equation of state). Thus, even at early times, diffusion is strong enough to thin the region of densest fluid for case F. The onset of instability increases the surface area across which diffusion takes place, and by roughly $t = 60$ s, the dense fluid all but disappears for case F [Fig. 12(c)]. In contrast, the dense fluid is dispersed, but does not fully disappear in Fig. 12(a). The cabbeling process leads to a production of dense fluid, and after around $t = 150$ s, a significant region of dense fluid occupies the bottom third of the domain. Subsequently, this region spreads upward, reaching roughly two-thirds of the domain by the end of the simulation. Contrasting Figs. 12(a) and 12(c) serves to make clear the stark contrast in late-time behavior for cases in which cabelling is present. If we consider fluid within 1% of the density maximum, as shown in Figs. 12(b) and 12(d), we see that the initial dynamics follow a similar pattern. Again, case F does not produce dense fluid at late times, whereas the cabbeling case does. However, the fraction of the domain at a given height occupied by this densest fluid is much smaller (up to 50% at some values of z) and is confined to within 0.01 m of the bottom boundary, as can be seen in Fig. 12(b).

Turning our attention exclusively to case CB, the spreading of the dense fluid in Fig. 12(a) is a result of increased mixing, while the shift to the bottom portion of the tank is a result of the feedback of cabbeling; this produces dense fluid that drives further sinking and, in turn, more mixing. The behavior of the densest fluid in Fig. 12(b) is, however, somewhat surprising: the three-dimensionalized instability is quite efficient at producing dense fluid, but not nearly as efficient at producing fluid that is very near the density maximum. One way this can be understood is as a result of the equation of state; the maximum density, $\rho(T^*)$, is the vertex of a parabola, and hence changes in T do not yield large changes in $\rho(T)$. In other words, while cabbeling in the three-dimensionalized state is a positive feedback mechanism, the nonlinear equation of state acts as a negative feedback mechanism, curtailing the production of the densest fluid. Another explanation, graciously provided by one of the anonymous reviewers, involves the fact that the overturning instability mixes together warm water from the lower part of the domain and cold water from the upper part, creating some intermediate fluid around the temperature of maximum density, T^*. The approach to the true value of T^* depends not only on the speed of this mixing process, but also on the tendency of this newly created fluid, which is higher in density than the parts which combined to form it, to sink out. Here we quote the reviewer directly: "In the present laminar scenario, the KH-like instability stops rather quickly and so mixing will be favoured only for a small period of time. If to this we add the fact that mixing of ρ in a state close to $T = T^*$ is slowed down because of the plateau in the equation of state, we see that this is why very little fluid (very) close to $\rho = \rho_{\max}$ is created before the fluid parcels have sunk to the bottom of the domain. This also explains why fluid with $\rho \approx \rho_{\max}$ is eventually created on long timescales but only at the bottom of the tank, where the heaviest fluid has ended up."

Figure 13 shows a comparison of the vertical and temporal distribution of the background [Fig. 13(a)] and perturbation [Fig. 13(b)] kinetic energy for cases F and CB. The difference of case F from case CB (which was shown in Fig. 11) is presented, with each panel scaled by the maximum value of the relevant quantity of the CB case. The background kinetic energy is seen to be larger in the F case by about 10%–15% over the majority of the water column. The perturbation kinetic energy is reduced by a similar amount during the main instability event for case F. For late times, the thin region near the top boundary of accelerated fluid is unique to the cabbeling regime (case CB). Thus, while the primary effect of cabbeling is on the density field, there is a smaller, but non-negligible, effect on the distribution of kinetic energy. Put another way, the positive feedback between mixing, the generation of dense fluid, and further mixing as that fluid sinks is unique to the cabbeling regime. This feedback has a weak expression in the kinetic energy, but is fundamental to the temperature (and hence density).

Figure 14 depicts the x-z profiles of the scaled spanwise averaged density, $\langle \rho \rangle_y$ for the basic cabbeling shear instability, case CB, and the no cabbeling case, F, which has the same density profile

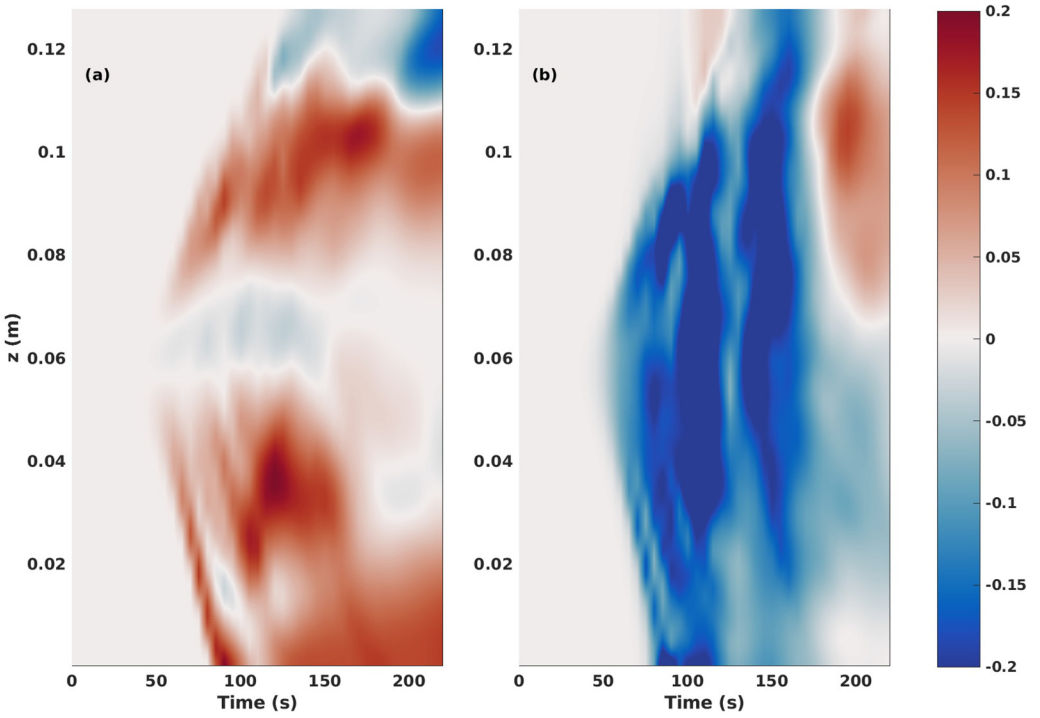

FIG. 13. (a) The difference in the horizontally averaged background kinetic energy, $\langle ke_{u_b}\rangle_{xy}(z,t)$, between cases F and CB, scaled by the maximum value of $\langle ke_{u_b}\rangle_{xy}(z,t)$ in the CB case. (b) The difference in the horizontally averaged perturbation kinetic energy, $\langle ke_{u_bp} + ke_v + ke_w\rangle_{xy}(z,t)$, between cases F and CB, scaled by the maximum value of $\langle ke_{u_p} + ke_v + ke_w\rangle_{xy}(z,t)$ in the CB case.

but a different temperature profile [see Eq. (19)]. Case CB is shown in the left column, whereas case F is shown in the right column. In both cases, the instability is initialized from the same shear flow (refer to Tables I and II for dimensional and dimensionless parameters). Note that the two cases have been scaled by their respective density ranges, such that a direct panel by panel comparison can be made.

During its early evolution, the cabbeling regime has a slightly higher concentration of dense fluid within the shear layer, as can be seen by comparing Figs. 14(a) and 14(b). This is a result of the non-negligible effect of diffusion in case F, which is due to its smaller temperature range (see Fig. 1 for a diagram of this). As the instabilities evolve, the dynamics of case CB lead to the generation of significantly more dense fluid than case F. Most stark is the contrast between Figs. 14(e) and 14(f), which serves to make clear that in the fully three-dimensionalized state, cases with and without cabbeling exhibit fundamentally different density distributions. Indeed, the two cases fail to track as they reach a fully three-dimensionalized state (after $t = 100$ s).

Given the lack of clear observations on current strengths and shear layer thickness during the early spring period in ice-covered lakes, it is important to ascertain the extent to which the results discussed above remain consistent as the Reynolds number is varied. While the range of possible density variations is largely set by the equation of state in the cabbeling regime (see Fig. 1), the natural parameter to vary is the strength of the initial shear current, or Δu. As such, Fig. 15 plots the perturbation kinetic energy components for various cases (considering changes to the Reynolds number), scaled by the initial nonzero component of the kinetic energy based on the background shear flow, $KE_{u_b}(0)$, specific to the case in question. Figures 15(a)–15(c) correspond to cases with cabbeling (CBH, CB, and CBD), whereas Figs. 15(d)–15(f) represent the fit (no cabbeling) cases

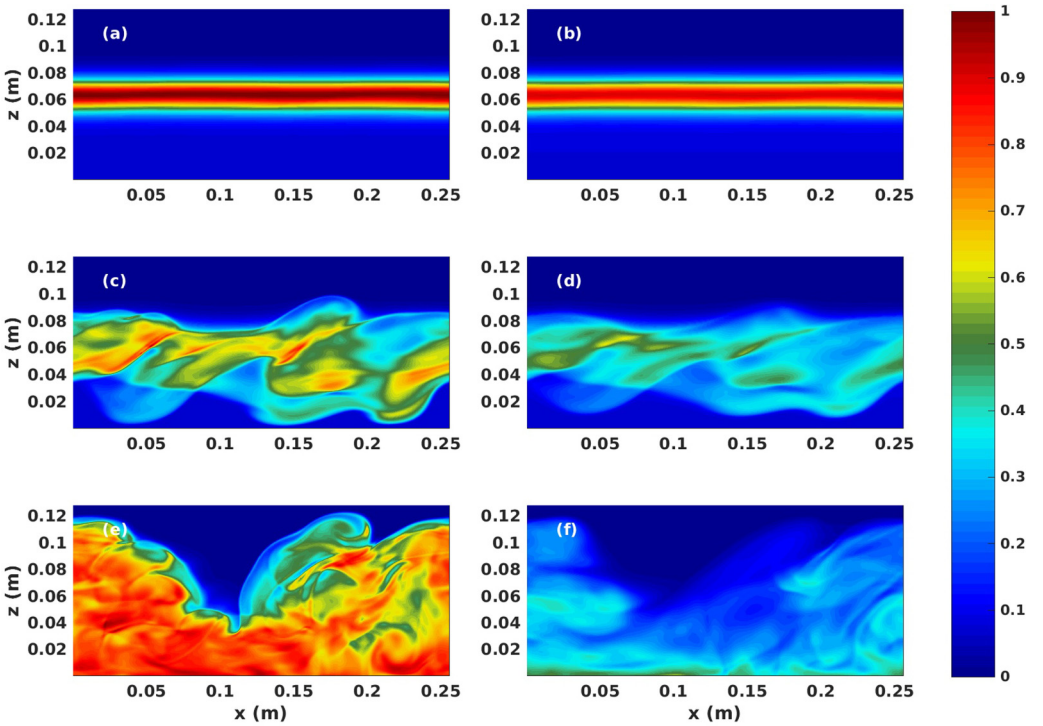

FIG. 14. x-z profiles of the spanwise averaged density, $\langle\rho\rangle_y(z,t)$ for the CB case (left column) and F case (right column) at times (a), (b) $t = 40$ s, (c), (d) $t = 80$ s, and (e), (f) $t = 120$ s. Since the range of densities is different for the two cases, we have shifted by the minimum density at $t = 0$ s and scaled by the range of densities so that the range is [0,1].

(FH, F, FD). From left to right (in both regimes) the panels correspond to the half strength initial shear ($\Delta u = 0.005$ ms^{-1}), the base case shear flow ($\Delta u = 0.01$ ms^{-1}), and the double strength initial shear ($\Delta u = 0.02$ ms^{-1}). In other words, the Reynolds number associated with the flow increases as we move to the right between panels. Figure 15 clearly demonstrates that the instability is less efficient at taking energy out of the background current as the current increases. Across all panels, the energy associated with the spanwise component, KE_v, is the smallest, though for the highest Reynolds number, this difference decreases. For cases CBH and FH [Figs. 15(a) and 15(d)] KE_w is the largest component, with a larger difference when cabbeling is present. The distribution of kinetic energy components in Fig. 15(a) mimics the behavior of the RT instability, where the peak of KE_w is considerably larger than the remaining components [compare to Fig. 10(c)]. This resemblance is highlighted again in Fig. 17 and is commented on in the accompanying discussion below.

Considering we are not in a fully turbulent regime, it becomes important to understand how the density is distributed throughout the domain as the Reynolds number varies. This is especially so since it was the density field (as opposed to the kinetic energy field) that was profoundly different when comparing the cabbeling, or CB, cases to the noncabbeling, or F, cases. Figure 16 shows the CB cases with Reynolds number increasing with row number: 16(a)–16(c) CBH, 16(d)–16(f) CB, and 16(g)–16(i) CBD. The figure depicts the simulations during their most vigorous period of 3D activity, for the leftmost, middle and rightmost columns, $t = (120$ s, 145 s, 170 s), respectively. A common feature between all three cases is an evolution toward a thin layer of light fluid near the upper boundary, below which is a well (though not completely) mixed region of dense fluid. Figures 16(a)–16(c) represent the lowest Reynolds number case and, apart from an increase of

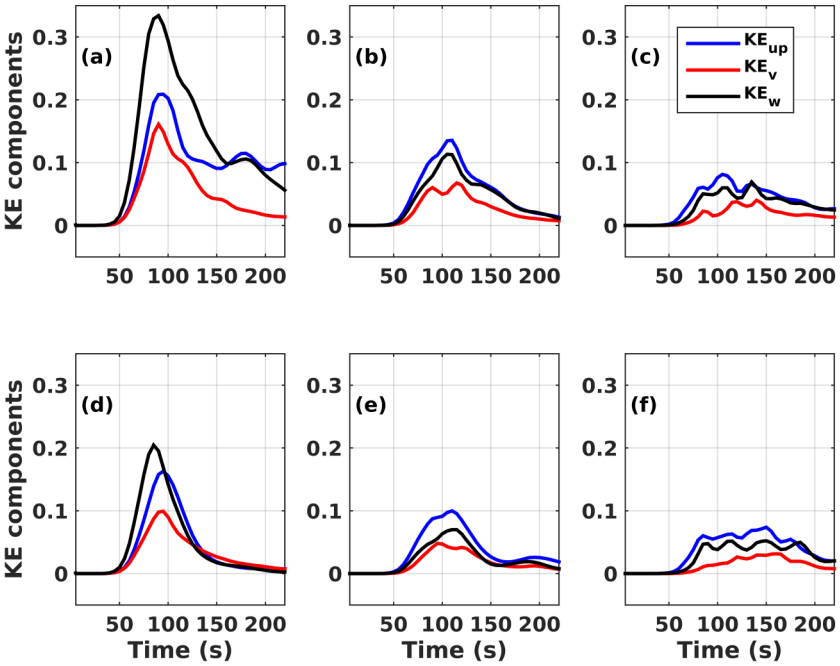

FIG. 15. KE components in the (a) CBH case, (b) CB case, (c) CBD case, (d) FH case, (e) F case, and (f) FD case. All panels are scaled by the corresponding value of $KE_{u_b}(0)$ for that case.

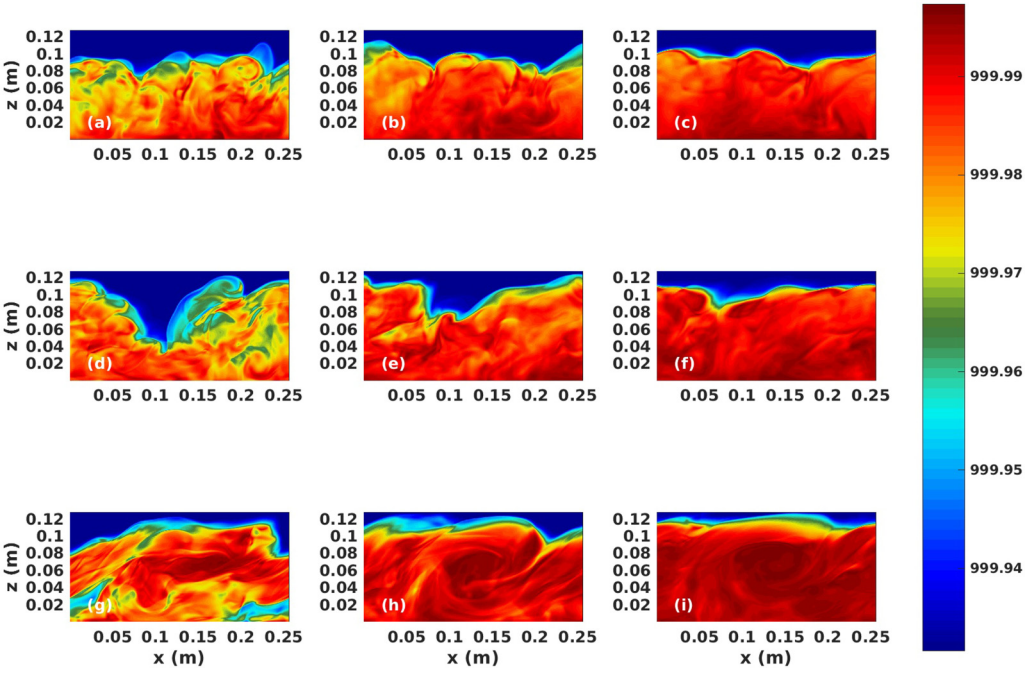

FIG. 16. The evolution of the spanwise averaged density, $\langle \rho \rangle_y(z,t)$ of the CBH case at (a) $t = 120$ s, (b) $t = 145$ s, (c) $t = 170$ s, the CB case at (d) $t = 120$ s, (e) $t = 145$ s, (f) $t = 170$ s, and the CBD case at (g) $t = 120$ s, (h) $t = 145$ s, (i) $t = 170$ s. All cases have a colorbar set by the range of density at $t = 0$ s.

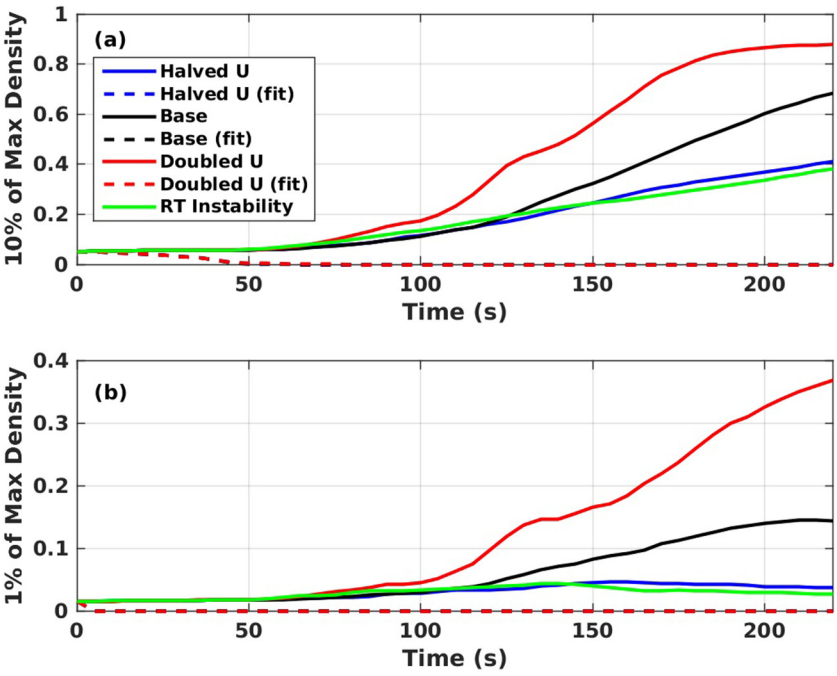

FIG. 17. Time series of the fraction of volume occupied by water within a fixed percentage of the maximum density (a) $CB_{10}(t)$ and (b) $CB_1(t)$. Legend provides a description of cases shown. CB cases shown as solid lines, F cases as dashed lines. The exceptional RT case is shown in green.

mixing in the thick lower layer, are relatively similar. When the initial shear, or Reynolds number, is increased by a factor of two ($\Delta u = 0.01$ ms^{-1}), there are significant differences between Figs. 16(d) and 16(f). The interface between the thin upper layer and the thicker lower layer remains dynamic until at least $t = 145$ s. When the the initial shear, or Reynolds number, is increased by a factor of two again [Figs. 16(g)–16(i)], the lower well-mixed region is seen to contain a relatively coherent vortex near the center of the domain [Figs. 16(h) and 16(i)]. We have confirmed that this vortex is associated with a billow pairing and indeed that a form of this pairing is observed in the corresponding case without cabbeling, FD. Cabbeling is thus not a necessary condition for its formation. Nevertheless, this structure serves to make clear that increasing the strength of the initial shear, or Reynolds number, does in fact have notable implications on the cabbeling regime. For the moderate range of Reynolds numbers studied, and in contrast with high Reynolds number KH or Holmboe instabilities, coherent structures persist well into the three-dimensionalized state of the instability. As a general comment, increasing the initial shear, or Reynolds number, leads to the generation of even more dense fluid, something that will be quantified next.

Given that the primary differences in the cabbeling, or CB, cases and the noncabbeling, or F, cases is observed in the density field, the volumetric fractions occupied by dense fluid within 10%, $CB_{10}(t)$, and 1%, $CB_1(t)$, of the density maximum provide us with the simplest way in which to compare quantitatively between cases. Figure 17 shows $CB_{10}(t)$ [Fig. 17(a)] and $CB_1(t)$ [Fig. 17(b)] for all six cases that varied the Reynolds number discussed above, with the additional consideration of the RT instability (case RT in Tables I and II). The most obvious observation to make is that all F cases lead to a monotonic decrease in CB_{10} [the same would be observed for CB_1 were we to focus in on the lower portion of Fig. 17(b)]. The next observation to note is that the RT case is quite similar to the CBH case. This is interesting given the profound difference in the primary form of the instability in these two cases (case CBH begins its life cycle as a shear instability while case RT

does not). Finally, we can note that an increase in initial shear, or equivalently Reynolds number, leads to a more rapid increase in both CB_{10} and CB_1. For the highest Reynolds number case (red curve) we can see that CB_{10} saturates near 0.9 while CB_1 is still increasing at the time the simulation is terminated.

IV. DISCUSSION

We have documented the nature of the three-dimensionalization of shear instability at moderate Reynolds number in the cabbeling regime of freshwater. In nature, this situation is realized in temperate lakes during early spring. Our parameter regime is representative of reported current strengths and length scales in lakes covered by ice, for which solar radiation is able to penetrate to a significant depth. As this is a difficult environment to perform measurements in, there is significant uncertainty in the parameter values. Nevertheless, the major conclusions of what we have shown above were found to be robust when the Reynolds number was either increased or decreased by a factor of two.

We find that the initial instability, which is a combination of KH-like shear instability and RT instability, is controlled by the initial profiles of density and velocity, and hence largely unaffected by cabbeling. This was demonstrated by creating a density profile for warm water (i.e., outside of the cabbeling regime) that matched the density of the one in the cabbeling regime (up to an additive constant). Cabbeling was, however, essential in the fully three-dimensionalized regime of the instability. All cases with cabbeling led to a state in which the majority of the water column was within 10% of the density maximum. A thin region of lower density fluid remained near the upper boundary and was only gradually worn away. In the high-density region, mixing was observed to be incomplete, even at late times. This is due to the nonlinearity of the equation of state; in this parameter region, density is a weakly varying function of temperature.

This is summarized in Fig. 18, which shows the horizontally averaged temperature field, $\langle T \rangle_{xy}$ [Eq. (16)]. In order to show both cases in the cabbeling regime (CB and CBD) and outside the cabbeling regime (case F), we have scaled by the initial temperature range. The strongest contrast is between case F Fig. 18(c)] and the cabbeling cases. However, the contrast is only dominant in the fully three-dimensionalized state (after $t = 100$ s). By comparing Figs. 18(a) and 18(b), it can be seen that the behavior of the cabbeling shear instability is robust over a significant range of Reynolds numbers, with some differences in the details (e.g., the region of light fluid near the top boundary is thinner for the higher Reynolds number, CBD case). By contrasting with the RT instability shown in Fig. 18(d), we see that the introduction of shear leads to greater irregularity and a more complete mixing over a larger portion of the water column. It is interesting to contrast Fig. 18(d) with the continuously stratified RT instability recently discussed in [29], their Fig. 9 [29] in particular. By doing this, it can be seen that cabbeling leads to an asymmetric temperature profile as the instability reaches a mature, 3D state.

The cabbeling regime is one of very small density changes (or very small Atwood number), occupying a parameter regime with weaker stratification than published literature on the three-dimensionalization of the Holmboe instability [30] or stratified KH instability [20]. It is thus a natural question to ask whether the stratification is anything more than a passive tracer in our context. Our stability analysis demonstrated that the initially unstable stratification (due to the nonmonotonicity of the equation of state) leads to a shift of the fastest growing unstable mode to higher wave numbers. Moreover,the case labeled KH, which has no density change, did not three-dimensionalize over the timescale of all other simulations (classical, 2D billows were observed instead). Thus, the small density differences are vital in setting both the length scale of, and the route to, three-dimensionalization of the instability.

By considering the kinetic energy split into a background and perturbation part [Eqs. (6) and (7)], we found that as the magnitude of the initial shear flow increases (equivalently increased Reynolds number) the instability is less efficient at extracting energy from the background shear. For the weakest initial shear, the vertical currents were found to dominate the perturbation kinetic energy,

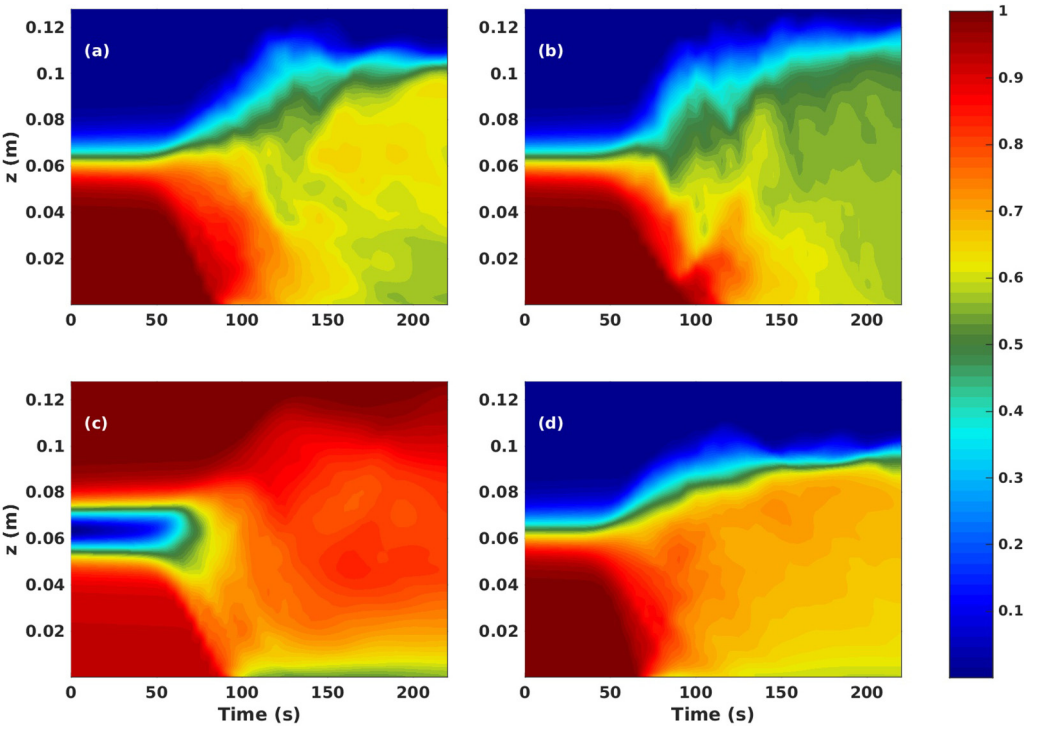

FIG. 18. The horizontally averaged temperature, $\langle T \rangle_{xy}(z, t)$, scaled by the range of temperatures at $t = 0$. The panels correspond to the (a) CB case, (b) CBD case, (c) F case (with the same initial shear flow as the CB case), and (d) RT case.

consistent with the RT instability in its mature form. As the magnitude of the initial shear flow was increased, the vertical and streamwise components of the kinetic energy were found to reach similar levels, with the spanwise component at roughly half their values. Thus, the observed behavior is somewhat different to that observed in high Reynolds number, stably stratified shear instability of either KH or Holmboe type. It also suggests that the 3D state of the shear instability in the cabbeling regime is not classical turbulence. Nevertheless, the period of strong three-dimensionalization lasts approximately 60 s in the simulations.

Future theoretical work should consider explorations of the quasi-turbulent state, especially as the Reynolds number increases. Analysis via detailed vorticity/enstrophy budgets and coherent structure methods (Q and R analysis) should further quantify the nature of the quasiturbulent state. A large eddy simulation (LES) diagnostic analysis, like that in [31], is also a clear avenue for future work. Applied future work should attempt to extract information from field data (e.g., [15]). A particularly poignant question is how do the conditions for shear instability in the cabbeling regime develop in the natural world (e.g., due to wind stress).

ACKNOWLEDGMENTS

This work was supported by the Natural Sciences and Engineering Research Council of Canada (NSERC) through Discovery Grant RGPIN-311844-37157. In addition, T.H. received financial support from the NSERC CGS M scholarship. The constructive comments of two anonymous referees greatly improved the manuscript.

[1] P. Hazel, Numerical studies of the stability of inviscid stratified shear flows, J. Fluid Mech. **51**, 39 (1972).
[2] G. P. Klaassen and W. R. Peltier, The influence of stratification on secondary instability in free shear layers, J. Fluid Mech. **227**, 71 (1991).
[3] R. T. Pierrehumbert and S. E. Widnall, The two- and three-dimensional instabilities of a spatially periodic shear layer, J. Fluid Mech. **114**, 59 (1982).
[4] A. Mashayek and W. R. Peltier, The zoo of secondary instabilities precursory to stratified shear flow transition. Part 2. The influence of stratification, J. Fluid Mech. **708**, 45 (2012).
[5] A. Lefauve, J. L. Partridge, Q. Zhou, S. B. Dalziel, C. P. Caulfield, and P. F. Linden, The structure and origin of confined Holmboe waves, J. Fluid Mech. **848**, 508 (2018).
[6] A. K. Kaminski and W. D. Smyth, Stratified shear instability in a field of pre-existing turbulence, J. Fluid Mech. **862**, 639 (2019).
[7] E. W. Tedford, R. Pieters, and G. A. Lawrence, Symmetric Holmboe instabilities in a laboratory exchange flow, J. Fluid Mech. **636**, 137 (2009).
[8] H. Salehipour, C. P. Caulfield, and W. R. Peltier, Turbulent mixing due to the Holmboe wave instability at high Reynolds number, J. Fluid Mech. **803**, 591 (2016).
[9] H. Van Haren and L. Gostiaux, A deep-ocean Kelvin-Helmholtz billow train, Geophys. Res. Lett. **37**, L03605 (2010).
[10] E. W. Tedford, J. R. Carpenter, R. Pawlowicz, R. Pieters, and G. A. Lawrence, Observation and analysis of shear instability in the Fraser River estuary, J. Geophys. Res.: Oceans **114**, C11006 (2009).
[11] W. D. Smyth, J. D. Nash, and J. N. Moum, Self-organized criticality in geophysical turbulence, Sci. Rep. **9**, 3747 (2019).
[12] S. Groeskamp, R. P. Abernathey, and A. Klocker, Water mass transformation by cabbeling and thermobaricity, Geophys. Res. Lett. **43**, 10,835 (2016).
[13] M. J. Andrews and S. B. Dalziel, Small Atwood number Rayleigh-Taylor experiments, Philos. Trans. R. Soc. A **368**, 1663 (2010).
[14] G. Kirillin, M. Leppäranta, A. Terzhevik, N. Granin, J. Bernhardt, C. Engelhardt, T. Efremova, S. Golosov, N. Palshin, P. Sherstyankin, G. Zdorovennova, and R. Zdorovennov, Physics of seasonally ice-covered lakes: A review, Aquatic Sci. **74**, 659 (2012).
[15] B. Yang, J. Young, L. Brown, and M. Wells, High-frequency observations of temperature and dissolved oxygen reveal under-ice convection in a large lake, Geophys. Res. Lett. **44**, 12,218 (2017).
[16] J. W. Cooper, Natural convection in a horizontal layer of water cooled from above to near freezing, J. Heat Transf. **97**, 47 (1975).
[17] P. Vasseur and L. Robillard, Transient natural convection heat transfer in a mass of water cooled through 4 °C, Int. J. Heat Mass Transfer **23**, 1195 (1980).
[18] D. S. Lin and M. W. Nansteel, Natural convection heat transfer in a square enclosure containing water near its density maximum, Int. J. Heat Mass Transf. **30**, 2319 (1987).
[19] H. N. Ulloa, K. B. Winters, A. Wüest, and D. Bouffard, Differential heating drives downslope flows that accelerate mixed-layer warming in ice-covered waters, Geophys. Res. Lett. **46**, 13872 (2019).
[20] C. P. Caulfield and W. R. Peltier, The anatomy of the mixing transition in homogeneous and stratified free shear layers, J. Fluid Mech. **413**, 1 (2000).
[21] L. N. Thomas and C. J. Shakespeare, A new mechanism for mode water formation involving cabbeling and frontogenetic strain at thermohaline fronts, J. Phys. Oceanogr. **45**, 2444 (2015).
[22] B. Akula, P. Suchandra, M. Mikhaeil, and D. Ranjan, Dynamics of unstably stratified free shear flows: An experimental investigation of coupled Kelvin–Helmholtz and Rayleigh–Taylor instability, J. Fluid Mech. **816**, 619 (2017).
[23] B. J. Olson, J. Larsson, S. K. Lele, and A. W. Cook, Nonlinear effects in the combined Rayleigh-Taylor/Kelvin-Helmholtz instability, Phys. Fluids (1994) **23**, 114107 (2011).
[24] P. K. Kundu, I. M. Cohen, and H. H. Hu, *Fluid Mechanics* (Academic Press, New York, 2002), p. 730.
[25] D. Brydon, S. Sun, and R. Bleck, A new approximation of the equation of state for seawater, suitable for numerical ocean models, J. Geophys. Res. **104**, 1537 (1999).
[26] C. J. Subich, K. G. Lamb, and M. Stastna, Simulation of the Navier-Stokes equations in three dimensions with a spectral collocation method, Int. J. Numer. Methods Fluids **73**, 103 (2013).

[27] Q. Lian, W. D. Smyth, and Z. Liu, Numerical computation of instabilities and internal waves from in situ measurements via the viscous Taylor–Goldstein problem, J. Atmos. Ocean. Technol. **37**, 759 (2020).
[28] L. N. Trefethen, *Spectral Methods in MatLab* (Society for Industrial and Applied Mathematics, Philadelphia, PA, 2000).
[29] J. Olsthoorn, E. W. Tedford, and G. A. Lawrence, Diffused-interface Rayleigh-Taylor instability with a nonlinear equation of state, Phys. Rev. Fluids **4**, 094501 (2019).
[30] W. D. Smyth and K. B. Winters, Turbulence and mixing in Holmboe waves, J. Phys. Oceanogr. **33**, 694 (2003).
[31] S. Khani and M. L. Waite, Large eddy simulations of stratified turbulence: The dynamic Smagorinsky model, J. Fluid Mech. **773**, 327 (2015).